



# GPS observed horizontal ground extension at the Hutubi (China) underground gas storage facility and its application to geomechanical modeling for induced seismicity

Guoyan Jiang<sup>a,\*</sup>, Xuejun Qiao<sup>b</sup>, Xiaoqiang Wang<sup>c</sup>, Renqi Lu<sup>d</sup>, Lin Liu<sup>a</sup>, Hongfeng Yang<sup>a</sup>, Yuanda Su<sup>e</sup>, Lili Song<sup>f</sup>, Baoshan Wang<sup>f</sup>, Teng-fong Wong<sup>a</sup>

<sup>a</sup> Earth System Science Programme, The Chinese University of Hong Kong, Hong Kong, China

<sup>b</sup> Institute of Seismology, China Earthquake Administration, Wuhan, China

<sup>c</sup> Xinjiang Earthquake Administration, Urumqi, China

<sup>d</sup> Institute of Geology, China Earthquake Administration, Beijing, China

<sup>e</sup> School of Geoscience, China University of Petroleum, Qingdao, China

<sup>f</sup> Institute of Geophysics, China Earthquake Administration, Beijing, China

## ARTICLE INFO

### Article history:

Received 2 August 2019

Received in revised form 23 October 2019

Accepted 1 November 2019

Available online 15 November 2019

Editor: R. Bendick

### Keywords:

underground gas storage  
horizontal ground extension  
induced seismicity  
geomechanical modeling  
physical mechanism

## ABSTRACT

Induced earthquakes and ground displacements were seldom reported in relation to gas injection or extraction. The Hutubi underground gas storage (HUGS) facility is the largest one in China and is also a unique case with both earthquakes and ground displacements detected during multiple cycles of injection and extraction since 9 June 2013. Unlike previous studies with a primarily seismological focus, here, we conducted quantitative analysis on the geomechanics of seismicity induced by the HUGS through developing a hydrogeologic framework, which systematically integrated geodetic, geophysical and geological data. First, we measured horizontal ground extension and shortening on the order of cm in response to gas injection and extraction of the HUGS at depth using a local GPS network, which was not reported in other regions with induced seismicity. Second, we synthesized a variety of data, including seismic reflection profiles, a newly acquired local velocity model, rock physics measurements, well drilling and logging data, to build up a 2D geomechanical model for the HUGS. Third, based on fully-coupled poroelasticity, we proposed two methods to optimize the permeability of the upper aquifers as well as the reservoir porosity and permeability with constraints from well level, GPS and well pressure data. Numerical simulations using the calibrated 2D model revealed that the horizontal extension due to the reservoir dilation is larger than ground uplift. The observed seismicity on faults without hydraulic connections to the gas repository was probably induced by the poroelastic effect of reservoir dilation. Our study provided a prototype scheme for detecting and characterizing the geomechanical behavior of cyclic fluid injection and extraction in a deep reservoir, which would be applicable to other UGS facilities.

© 2019 Elsevier B.V. All rights reserved.

## 1. Introduction

There have been numerous reports of earthquakes induced by anthropogenic activities, including wastewater disposal (e.g., Keranen et al., 2014; Skoumal et al., 2014), injection of CO<sub>2</sub> for enhanced oil recovery and geologic sequestration (e.g., Gan and Frohlich, 2013; Verdon et al., 2013), hydraulic fracturing (e.g., Bao and Eaton, 2016; Schultz et al., 2018), and enhanced geothermal systems (e.g., Majer et al., 2007). In particular, a number of relatively large earthquakes in the past decade have been attributed

to fluid injection in petroleum fields, which have motivated extensive seismological, hydrogeological and geomechanical investigations into the physical processes of induced seismicity (Keranen and Weingarten, 2018). In comparison, fewer earthquakes have been reported in relation to gas injection or production as well as cyclic gas injection–extraction (Foulger et al., 2018).

Gan and Frohlich (2013) identified a cluster of seismic events possibly triggered by CO<sub>2</sub> injection in a Texas oil field. They underscored many critical questions that remain unanswered on how earthquakes are induced by gas injection, which they emphasized cannot be addressed solely by seismological observations but requires complementary investigations of hydrogeology and subsurface stress. Another well-documented case related to gas injection

\* Corresponding author.

E-mail address: guoyanjiang@gmail.com (G. Jiang).

is the CO<sub>2</sub> storage project in Weyburn, Alberta, where tens of microearthquakes were detected after installation of geophones in 2003. Since most of the events were located far from the injection well, Verdon et al. (2011) argued that such spatial distribution is in discrepancy with the conventional scenario of injection-induced seismicity as enumerated above, and they accordingly adopted a geomechanical model that couples the hydrological and poromechanical responses. The extraction of gas has also been reported to induce seismicity, such as the Groningen gas field in Netherlands (Thienen-Visser and Breunese, 2015). In the seminal analysis of related phenomena, Segall (1989) appealed to a coupled poromechanical model to elucidate the spatial distribution of stress and deformation.

Even less is known concerning seismicity that may be induced by cyclic injection and extraction of gas, which typically occurs on an annual basis in an underground repository. Hundreds of such storage facilities for natural gas have been established worldwide in depleted hydrocarbon reservoirs, aquifers and cavern formations (Foulger et al., 2018), which can effectively modulate the supply in response to seasonal demand, as well as reinforce national energy security. According to the global database of over 700 cases of induced earthquakes compiled by Foulger et al. (2018), only seven cases were likely associated with underground gas storage (UGS), two of which occurred recently in Spain and China. Located in depleted hydrocarbon reservoirs, both repositories commenced gas injection in 2013. The Hutubi underground gas repository in Xinjiang with a design capacity of 10.7 billion m<sup>3</sup>, about 8-fold larger than the capacity (1.3 billion m<sup>3</sup>) of the Castor project in Gulf of Valencia, is the largest among similar facilities in China.

However, the Castor project was stopped only after 12-day operation because seismicity was detected soon after gas injection. The seismicity was still ongoing and detected in 2016. Over 1000 earthquakes with the largest magnitude up to 4.3 occurred two weeks after the shutoff (Gaite et al., 2016; Foulger et al., 2018). Seismological data indicate that the seismicity was likely related to activation of the Amposta fault and other neighboring reservoir faults (Gaite et al., 2016). A coupled flow-geomechanics analysis suggests that the Amposta fault was destabilized by injection, whereas the neighboring faults might have been activated by poroelastic stress perturbation (Gaite et al., 2016; Juanes et al., 2017).

On the other hand, although geodetic approaches including Global Positioning System (GPS) and Interferometric Synthetic Aperture Radar (InSAR) have been widely used to measure the spatiotemporal evolution of ground deformation, surface displacements were only observed in several regions with induced seismicity (e.g., Mossop and Segall, 1997; Fialko and Simons, 2000; Barbour et al., 2016), especially in the regions with gas injection or extraction activities. Vasco et al. (2010) imaged double-lobe uplift at the CO<sub>2</sub> sequestration site of In Salah, Algeria, using InSAR. Thienen-Visser and Breunese (2015) reported that the surface subsidence in the Groningen gas field measured by leveling since 1964 was up to 30 cm.

Limited geodetic observations in the regions with induced seismicity led to fewer studies incorporating them into seismological and geomechanical analyses. The usefulness of such an integrated approach for seismicity induced by fluid injection was recently demonstrated by Shirzaei et al. (2016 and 2019), who applied a multitemporal InSAR approach to measure surface uplift due to wastewater disposal in eastern Texas and further inverted the hydraulic diffusivities and permeabilities of injection layers. For the cases with gas injection or extraction, Verdon et al. (2015) found that the InSAR measurements of surface uplift at In Salah seemed to correlate with limited seismicity data based on geomechanical modeling. In the Groningen gas field, the subsidence was interpreted with compaction models and then used to derive an em-

pirical relationship between cumulative compaction and seismic moment (Thienen-Visser and Breunese, 2015).

The Hutubi underground gas storage (HUGS) facility is a unique case with both induced earthquakes (Yang et al., 2017; Tang et al., 2018; Zhou et al., 2019) and potential surface displacements (Qiao et al., 2018) associated with cyclic gas injection-extraction. Tang et al. (2018) analyzed the seismological data of the Xinjiang seismic network from 9 June 2013 to 10 October 2015 and suggested that the seismicity likely occurred on pore-pressured faults governed by rate- and state-dependent friction and poroelastic responses to the abrupt changes in injection rate and well pressure. Zhou et al. (2019) conducted seismological analysis of data from a temporary network comprising 38 mobile stations as well as from the Xinjiang seismic network with a time span from 9 June 2013 to 31 December 2015. Accordingly, they were able to better resolve the location and spatial clustering of the events associated with the first and second injection phases, and most importantly, to derive the focal mechanism solutions of the two largest events in August 2013.

Both studies revealed that the HUGS had induced  $M_L > 3.0$  earthquakes. However, their conclusions on the physical mechanism of induced seismicity are different. Tang et al. (2018) argued that both pore pressure and poroelastic stress perturbation contributed to induce the events. In contrast, Zhou et al. (2019) regarded that poroelastic perturbation was the only mechanism responsible for the observed seismicity. In the absence of detailed hydrogeological and geomechanical modeling, the two distinct physical mechanisms were limited to qualitative conclusions. The first objective of our study is to fill this gap with quantitative understanding of the geomechanics of seismicity induced by the HUGS and to validate the two conclusions. Guided by a synthesis of seismic reflection profiles, a local velocity model, rock physics experiments, well drilling and logging data, we developed a hydrogeologic framework for a 2D geomechanical model that fully couples the hydrological and poroelastic processes. The new solutions of focal mechanism (Zhou et al., 2019) provided us with critical references for simulating the spatiotemporal evolution of Coulomb stresses.

In the aspect of surface deformation, an earlier analysis of the vertical deformation measured by both GPS and InSAR has demonstrated that its major contribution was from the hydrologic cycle and groundwater withdrawal, with little connection to gas injection or extraction (Qiao et al., 2018). Whether cyclic gas injection-extraction have induced detectable ground displacements is still in doubt. Meanwhile, comparing with the rocky, desert conditions at In Salah that are almost ideal for InSAR monitoring (Verdon et al., 2013), the HUGS site is covered by farmlands and vegetation, which tends to cause loss of interferometric coherence and limits the capability of InSAR approach. To circumvent these two technical challenges, we instead focused on horizontal GPS data of a local GPS network established in May 2013 (Fig. S1) to measure potential horizontal ground extension and shortening in response to gas injection and extraction of the HUGS at depth, which is the second objective of this study. Moreover, unlike previous studies with a primarily seismological focus, we also tried to develop a methodology to incorporate the potential horizontal GPS observations into geomechanical modeling of cyclic gas injection-extraction within the HUGS to derive quantitative constraints on the hydromechanical responses, especially of the reservoir layer.

## 2. Tectonic setting and operation of the HUGS

### 2.1. Tectonic setting

Our study region (Fig. 1a) is situated in the southern Junggar Basin, where the regional topography reveals several subparallel

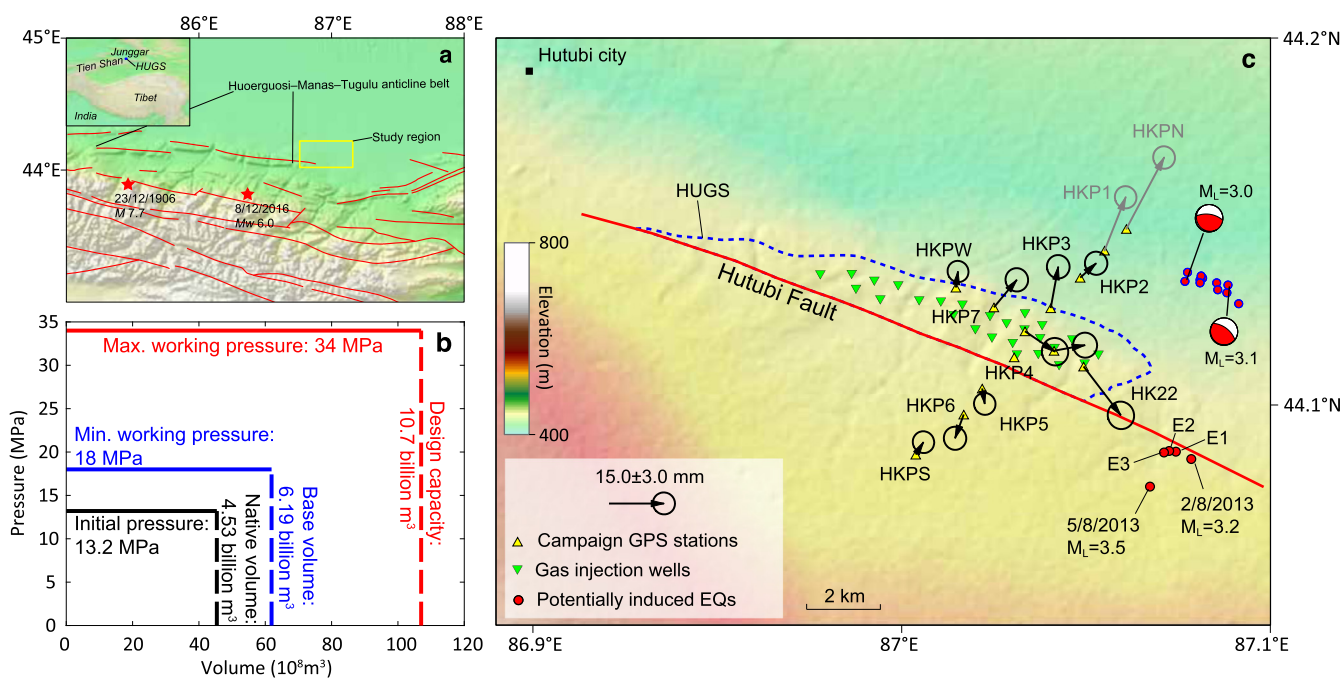


**Fig. 1.** The Hutubi underground gas storage facility. (a) Geological background. Red lines are active faults from the active tectonic map of China (Deng et al., 2007). Red stars locate the 1906 Mana and 2016 Hutubi earthquakes. (b) Relationship between gas volumes and wellhead pressure of the HUGS. (c) Observed horizontal ground extension from 28 March 2014 to 18 November 2017 and locations of induced earthquakes. Five red dots with black borders show the  $M_L \geq 3.0$  earthquakes (E1: 1/8/2013  $M_L = 3.0$ ; E2: 3/8/2013  $M_L = 3.6$ ; E3: 3/8/2013  $M_L = 3.0$ ) from Tang et al. (2018). The red points with blue borders mark the seismic cluster in August 2013 relocated by Zhou et al. (2019). The two largest events on 3 August are denoted with focal mechanisms. (For interpretation of the colors in the figure(s), the reader is referred to the web version of this article.)

and east-west trending thrust-fold belts formed since the Cenozoic Indo-Asian collision (e.g., Deng et al., 1994). Among them, the Huoerguosi-Manas-Tugulu anticline belt is the longest, whose easternmost part intersects with the study region. Present-day GPS velocity field shows that the study region is undergoing north-south shortening at rates of 2–5 mm/yr (Qiao et al., 2018). Active tectonics in the northern piedmont of the Tian Shan has resulted in many strong earthquakes (Deng et al., 1996; Wang et al., 2004), including two  $M \geq 6$  earthquakes in 1906 and 2016 (Fig. 1a), respectively. In a recent analysis of the seismotectonics of these two events, Lu et al. (2018) argued that both are connected to the Huoerguosi-Manas-Tugulu fault with a ramp-flat-ramp geometry.

In the foreland of the Junggar Basin, there are numerous structural traps holding hydrocarbon (Hu et al., 2010). The HUGS was transformed from one of the depleted reservoirs, which had been producing gas for about 14 yr from 1998 to 2012 (Pang et al., 2012). With an average thickness of  $\sim 110$  m, the sandstone reservoir is located at a central depth of  $\sim 3.6$  km, extending laterally over an area of  $\sim 12$  km  $\times$  2.6 km (Fig. 1c). As will be elaborated in Section 3.2, our interpretation of five seismic profiles reveals that the HUGS is located below the Hutubi anticline and bounded on one side by the northwest-trending Hutubi fault (Fig. 1c). This thrust fault dips towards the southwest at a relatively low angle of  $\sim 20^\circ$ . Field tests have shown that it has excellent sealing characteristics and acts as an effective barrier to gas transport (Pang et al., 2012).

## 2.2. Cyclic gas injection and extraction

To guarantee a stable gas supply for northern Xinjiang and strategic security of the West-East Gas Pipeline Network, PetroChina Xinjiang Oilfield Branch transformed the depleted Hutubi gas field into an underground gas repository. The designed minimum working gas volume and capacity are 6.19 and 10.7 billion  $m^3$  (Fig. 1b), respectively. To attain this lower threshold, 1.66 billion  $m^3$  of natural gas needs to be injected into the reser-

voir (Cao, 2013). By 1 June 2018, the HUGS has completed five injection-extraction cycles. In warm seasons, natural gas is injected into the reservoir, ready for supply in cold seasons. Between each injection and extraction phases, there is a balance phase lasting about three weeks for equipment maintenance.

As our 2D geomechanical model was developed with major reference to the seismic profile L290 based on the spatial distribution of GPS station (Fig. S1b), we collected production data of 11 wells surrounding the profile (Fig. 2a) from the HUGS operator. Figs. 2 and S2 show the wellhead pressure and gas injection-extraction rates, respectively. As the production rates were only available from 1 January 2015 to 30 April 2017, we had to collect some open reports on the total gas volume and time span of the first injection-extraction and second injection cycles to infer the rates (Table S1). Considering that the production rates varied appreciably among some wells, their mean values were used in Sections 5.2–5.4 to conduct geomechanical simulations. For comparison with predicted pore pressure changes, we also estimated the root-mean-square (RMS) error of the observed relative pressure changes, equal to 1.87 MPa. More information on the production data is provided in the Supplementary Material (SM-S2).

## 3. Geodetic, geophysical, and geological observations

### 3.1. GPS observed horizontal ground extension

Due to the reason of observation time span, we only used 13 campaign stations of the local GPS network to measure the cumulative horizontal ground displacements within five time periods (SM-S1). Figs. 1c and 3 show the horizontal displacements of the fifth and another four periods with reference to station HKP4 near the HUGS center, respectively. Two stations (HKP1 and HKPN) at the outskirts show displacements that are significant larger than the others, likely dominated by hydrological process rather than the HUGS operation (see more explanations in Sections 5.1 and 5.3). Excluding these two anomalous stations, three deformation pat-

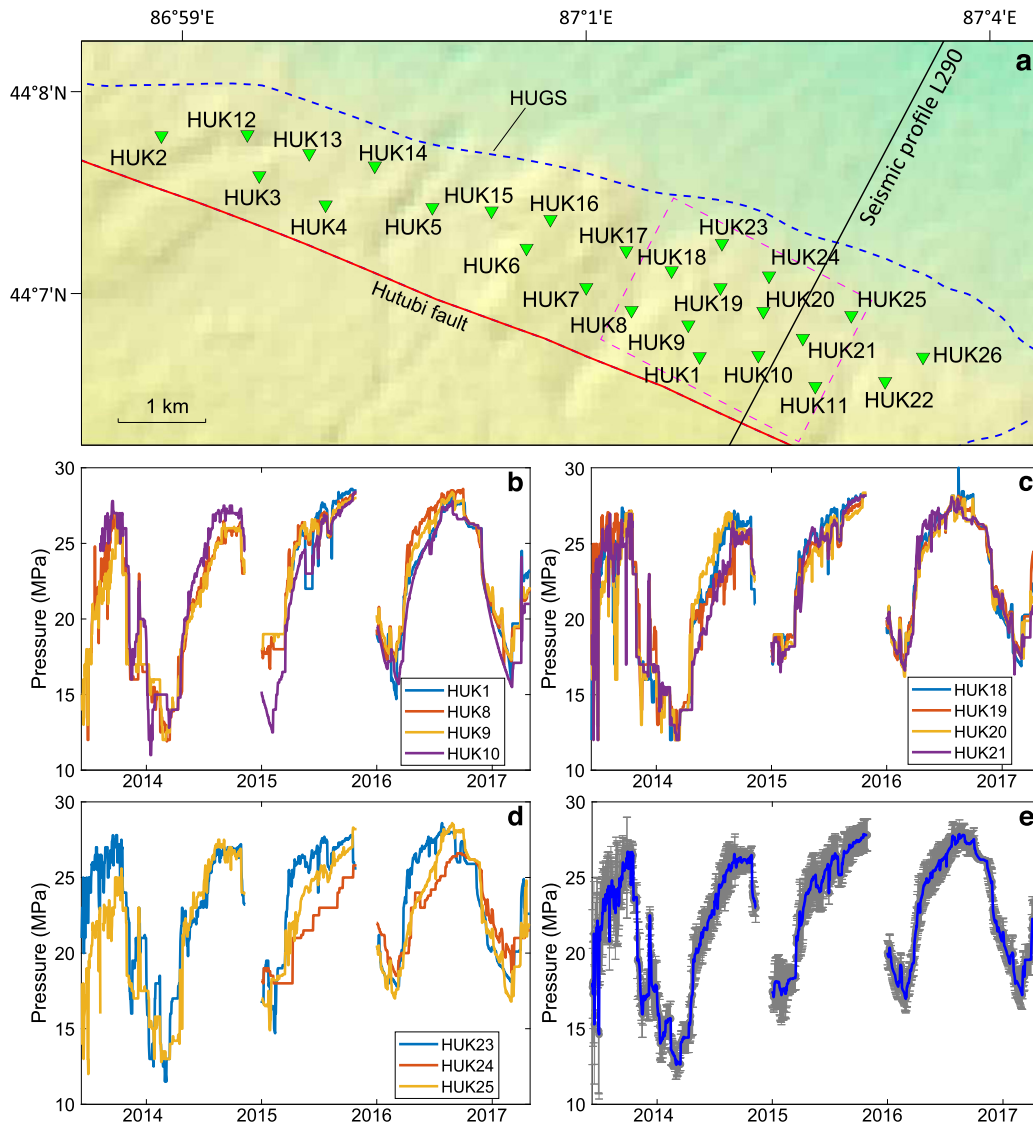


**Fig. 2.** Wellhead pressure data from 9 June 2013 to 30 April 2017. (a) Distribution of gas injection/extraction wells. Pink dashed rectangle outlines the 11 wells adopted in this study. (b-d) Observed wellhead pressure of the 11 wells surrounding the seismic profile L290. (e) Average wellhead pressure with daily uncertainties shown by gray error bars.

terns can be identified. First, the displacement magnitudes tend to be larger outside the HUGS, which is particularly evident in Figs. 1 and 3c with more injection phases than extraction phases. Second, injection or extraction results consistently in an extension or shortening that tends to be localized near the HUGS. This is best illustrated by comparing Figs. 3b and 3d with Fig. 3c. Third, the extension magnitudes increase during each gas injection phase and decrease during extraction phases. These spatiotemporal trends indicate that our GPS measurements of horizontal deformation are probably connected with the injection and extraction activities of the underground repository. Having GPS data from multiple annual cycles allows us to validate the consistency of responses from cycle to cycle, as well as the contrast between injection and extraction phases.

As the acquisition of production data is as of 30 April 2017 (Fig. 2), here we only used the observations in the four periods as shown in Fig. 3. The displacement vectors were further projected on the horizontal plane that contains the strike of the Hutubi fault, and two components perpendicular and parallel to the fault strike were resolved. As our geomechanical model mainly refers to the seismic profile L290, we only adopted the component perpendicular to the fault strike for comparison with model prediction (insets

in Fig. 3). The error bar of each station in the displacement profiles (after two processes of removing the regional deformation trend and projection) was derived using the measurement errors of two horizontal components. Furthermore, we estimated the RMS error of the extension data in the four profiles (excluding the two anomalous stations) to be 0.41 cm based on their uncertainties.

In all four periods, the displacement profiles show an overall extension trend that increase at distances away from the HUGS center (Fig. 3). The magnitude initially increased by as much as 10 mm over a distance of  $\pm 1$  km to attain a peak, then decayed at some distance from the HUGS. Because slope of such a curve corresponds to a linear strain, the implication is that our methodology has effectively resolved an extensional strain on the order of  $10^{-5}$  developed on the surface in response to injection of gas into the HUGS. Both magnitudes of the displacement and strain as well as their spatial distribution are in qualitative agreement with prediction of idealized models (e.g., Mogi, 1958) for injection and extraction of fluid in an elastic half-space. Sections 5.2 and 5.3 present a more quantitative analysis hinging on the development of a realistic hydrogeologic framework for a fully-coupled geomechanical model.

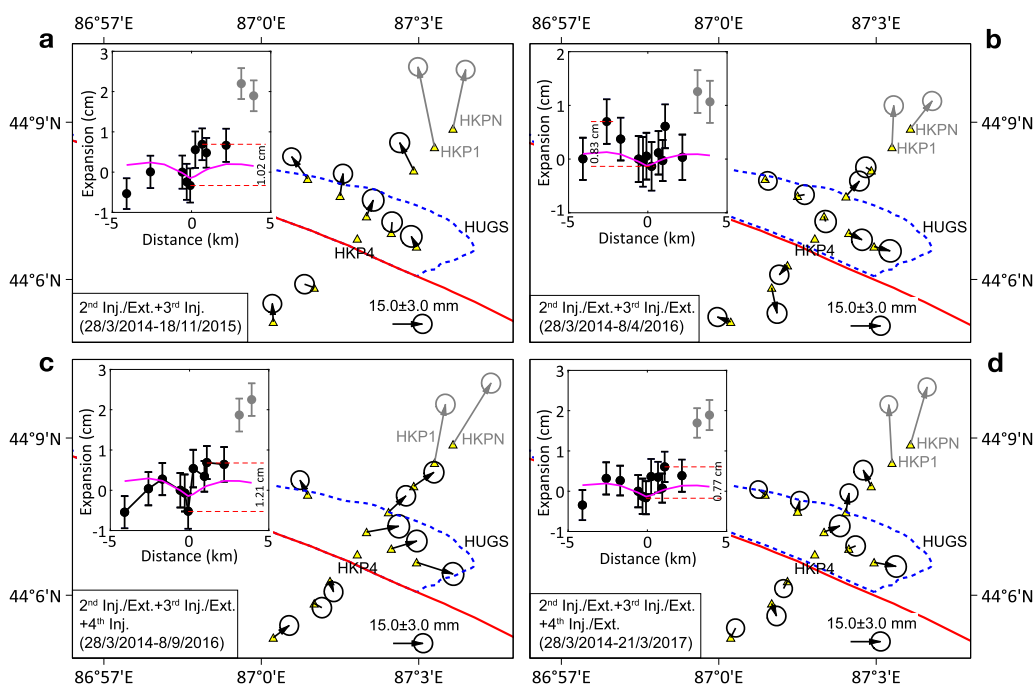


**Fig. 3.** GPS observed horizontal ground displacements relative to station HKP4 during four periods. The two stations in the northeast likely dominated by hydrological process are plotted with color gray. The inset in each panel shows the horizontal ground extension profiles in the horizontal direction perpendicular to the strike of the Hutubi fault. Lateral ground extension relative to the HUGS center is defined to be positive displacements. Two red dashed lines in each profile mark the observed maximum ground extension. Pink lines in the profiles are the simulated displacements under the preferred hydraulic parameters (porosity = 20%, permeability =  $3.25 \times 10^{-13} \text{ m}^2$ ) of the reservoir layer.

### 3.2. Seismic reflection profiles and drilling data

We have available from PetroChina five seismic reflection profiles, approximately equally spaced in the study area from southeast to northwest (Fig. S4). Three profiles (L150, L220, and L290) cut through the HUGS. Along profile L220 there is a well (DF1) with core samples and geologic log data. Together with two other wells (HU2 and HUK17) such data have provided important constraints on the stratigraphic column (Table S2).

We adopted the fault-related fold theory (Shaw et al., 2005) to interpret the seismic profiles (Figs. 4a-4e) and identified six faults (the Hutubi fault and Faults I-V). More details on the interpretation refer to SM-S3. Fig. 4f summarizes our stratigraphic and structural interpretation. Dip angle of the Hutubi fault with distinct thrust-slip feature ranges from  $20^\circ$  to  $25^\circ$ . Faults I and II dip to the northeast with angles varying from  $22^\circ$  to  $37^\circ$ . Faults III-V dip in a conjugate direction with angles between  $7^\circ$  to  $28^\circ$ . In contrast, previous studies interpreted another two faults (red dashed lines in Figs. 4c and 4d) (Pang et al., 2012; Cao, 2013). However, we observed no clear faulting features and thus did not consider them in our geomechanical model.

### 3.3. Active seismic source and borehole geophysics data

Near the GPS station HTBC at a distance of  $\sim 20$  km north of the HUGS is an active airgun source (Fig. S1a), which was monitored by 37 portable stations (Fig. S5a). To develop a local velocity model, Ji et al. (2017) analyzed the airgun signals recorded in May 2016 and used surface wave dispersion curves of the stacked signals to invert the shallow  $S$ -wave velocity structure with the software CPS330 (Herrmann, 2013). The  $P$ -wave velocities were then inferred from the velocity ratios between  $P$ - and  $S$ -waves of CRUST1.0 (Laske et al., 2013). The crustal density profile (Fig. S5b) was derived using a nonlinear empirical velocity-density formula (Brocher, 2005; Ludwig et al., 1970).

We also had access from the Xinjiang Branch of PetroChina Logging Company porosity profiles of nine wells at different depth ranges (Figs. S4 and S6), which have been derived from borehole geophysics data including acoustic, neutron, and density logs. For development of the hydrogeologic framework, we derived the mean and median porosities for several different depth ranges from histograms of the borehole data (Fig. S6).

## 4. Geomechanical modeling

### 4.1. Model setup

Guided by the geophysical and geological observations summarized in the previous section, we formulated a 2D geomechanical model for the HUGS with major reference to the seismic profile L290 based on the distribution of the 13 campaign GPS stations. Extending over a width of 36 km and a depth of 14 km, the model comprises seven layers: Upper Aquifers 1-2, Upper Layer 3, Caprock Layer, Reservoir Layer, and Basal Layers 1-2 (Fig. 5). At the HUGS center, the reservoir layer extends from a depth of 3.53 km to 3.64 km. With a width of 2.2 km, the repository is bounded on the southwest by the Hutubi fault, which is approximated in the model as impermeable (with a thickness of 10 m) based on previous field tests and operation of the gas field (Pang et al., 2012). The northeast boundary corresponds to the gas-water interface, also treated as impermeable in our model.

The porous medium in our model was assumed to be isotropic and linearly poroelastic, and for each layer and faults we needed to specify its elastic moduli, porosity and permeability (Table 1). The elastic moduli of the seven layers were calculated based on the local velocity and density profiles (Fig. S5). The porosity value of each layer was estimated based on the logging data (Fig. S6), stratigraphy (Table S2) and observations on core samples from outcrops (Table S3). Unlike the elastic moduli and porosity, permeability variation among the layers is difficult to constrain. We conducted careful analysis of hydrogeological units in the study

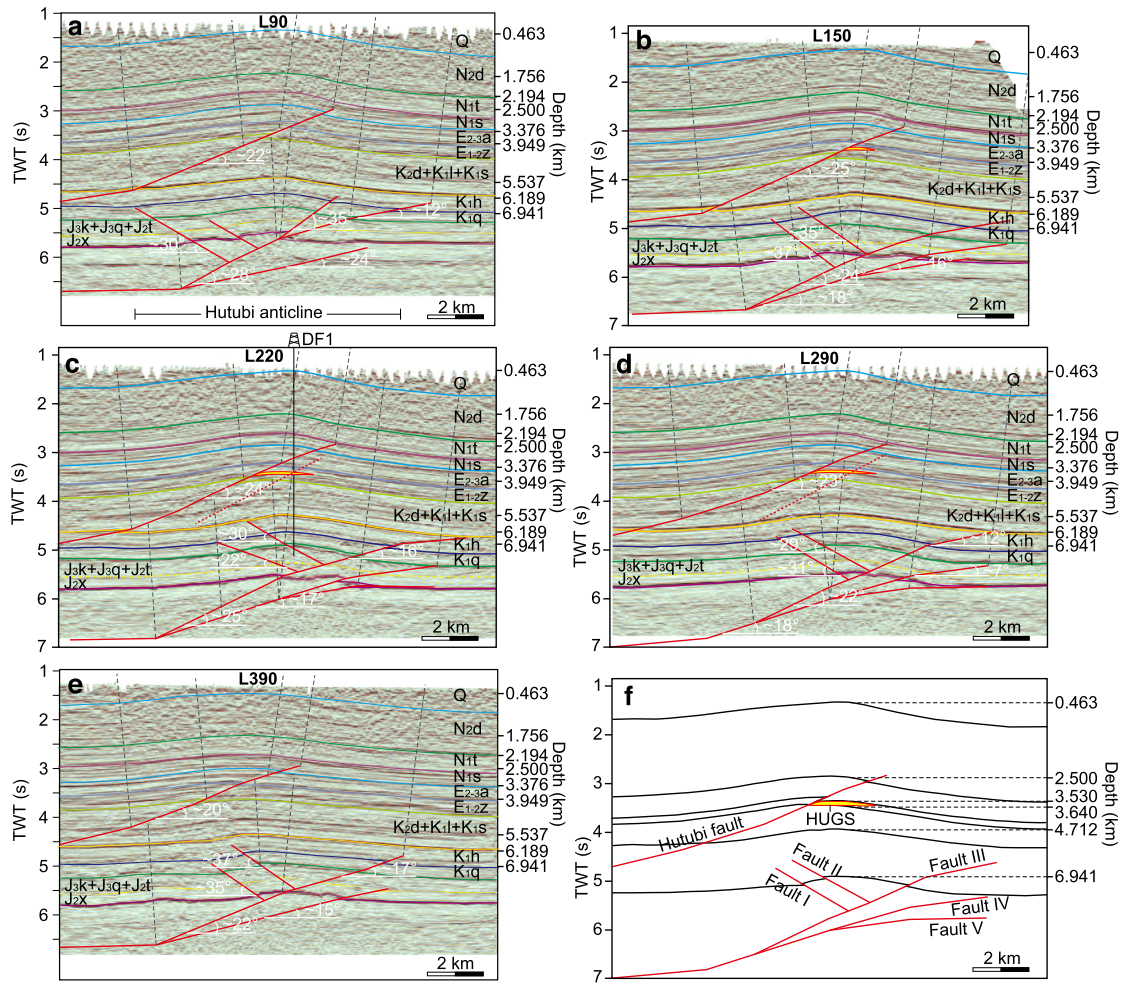


**Fig. 4.** Geological interpretation of five seismic profiles. Their locations are shown in Figure S4. (a-e) Seismic profiles with interpretation results of faults (red lines) and stratigraphic division. Explanation of strata codes refers to Table S2. Two red dashed lines in panels (c) and (d) show the faults identified by Pang et al. (2012) and Cao (2013). Well DF1 with drilling data is located in profile L220. (f) Schematic diagram of simplified strata and fault distribution.

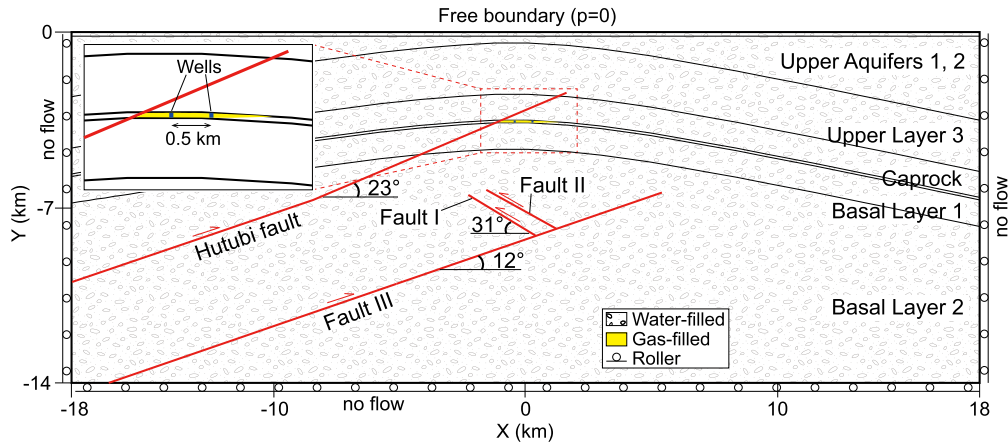


**Fig. 5.** Schematic description of the geomechanical model for the HUGS with boundary conditions. The ground surface boundary condition, pressure = 0, is only active for the simulation of cyclic gas injection-extraction rather than groundwater pumping. The model width and depth were set to be 36 km and 14 km, respectively, to minimize the boundary effects. Except for the repository that is saturated with gas, all rocks in the model are saturated with water.

area (SM-S4). Additionally, benefiting from the GPS data at station HP12 measuring aquifer uplift near water well H5 (Fig. S1b) and production data of the HUGS, we were able to further constrain the permeability of Upper Aquifers 1-2 as well as the hydraulic properties (porosity and permeability) of the reservoir layer in Sections 5.1 and 5.2, respectively.

#### 4.2. Finite element modeling based on fully-coupled poroelasticity

In a seismogenic system hydraulically connected to the injection sources, earthquakes can be induced solely by enhancement of pore pressure, and the mechanics may be analyzed simply by a hydrological model for pore pressure evolution, together with

**Table 1**

Mechanical and hydraulic parameters of the rock formations and faults in the geomechanical model for the HUGS and fluid properties.

| Layer              | Thickness (km)     | Density (kg/m <sup>3</sup> ) | Young's modulus (GPa) | Biot coefficient <sup>a</sup> | Poisson's ratio | Porosity (%)                  | Permeability (10 <sup>-15</sup> m <sup>2</sup> ) | Viscosity (Pa s)        | Compressibility (Pa <sup>-1</sup> ) |
|--------------------|--------------------|------------------------------|-----------------------|-------------------------------|-----------------|-------------------------------|--|-------------------------|-------------------------------------|
| Upper Aquifer 1    | 0.150              | 1132                         | 0.44                  | 0.98                          | 0.39            | 12                            | 13 or 75 <sup>c</sup>                            |                         |                                     |
| Upper Aquifer 2    | 0.313 <sup>b</sup> | 1681                         | 2.10                  | 0.91                          | 0.39            | 8                             |  |                         |                                     |
| Upper Layer 3      | 2.037              | 2038                         | 5.99                  | 0.76                          | 0.38            | 6                             | 0.2  |                         |                                     |
| Caprock Layer      | 1.030              | 2334                         | 21.06                 | 0.44                          | 0.32            | 2                             | 0.00001  |                         |                                     |
| Reservoir Layer    | 0.110              | 2362                         | 24.37                 | 0.39                          | 0.31            | 3~30<br>(20~30 <sup>d</sup> ) | 0.1~1000<br>(125~325 <sup>d</sup> )              |                         |                                     |
| Basal Layer 1      | 1.072              | 2394                         | 28.68                 | 0.32                          | 0.30            | 5                             | 0.001  |                         |                                     |
| Basal Layer 2      | 2.229              | 2488                         | 44.09                 | 0.09                          | 0.27            | 5                             | 0.01   |                         |                                     |
| Faults             | 0.010              | 2488                         | 10                    | 0.79                          | 0.27            | 5                             | 0.0001   |                         |                                     |
| Gas <sup>e</sup>   |                    | 154                          |                       |                               |                 |                               |  | 2.12 × 10 <sup>-5</sup> | 1 × 10 <sup>-5</sup>                |
| Water <sup>f</sup> |                    | 1000                         |                       |                               |                 |                               |  | 55 × 10 <sup>-5</sup>   | 0.42 × 10 <sup>-9</sup>             |

<sup>a</sup>Calculated based on the equation,  $\alpha = 1 - K/K_s$  (Wang, 2000), where  $K$  is the drained bulk modulus and  $K_s$  is bulk modulus with a fixed value of 35 GPa. More explanations refer to SM-S5.

<sup>b</sup>Thickness at the center of the HUGS.

<sup>c</sup>Constrained by water level changes of well H5 and vertical displacements at station HP12 (Section 5.1).

<sup>d</sup>Constrained by GPS-observed horizontal ground extension and wellhead pressure changes (Section 5.2).

<sup>e</sup>The density and viscosity of natural gas were obtained by averaging two groups of values retrieved from <https://checalc.com/solved/gasVisc.html> based on the reservoir temperature of 92.5°C (Cao, 2013) and two pressure values of 13.2 and 30 MPa, which correspond to the initial and expected maximum values of the reservoir. The compressibility is in line with the magnitude of CO<sub>2</sub> in Bjørnå et al. (2016) with the condition of T = 50 °C and P = 20 MPa.

<sup>f</sup>The water properties are also from Bjørnå et al. (2016).

mechanical consideration based on Terzaghi's effective stress principle. However, for the HUGS, previous seismological studies presented two different interpretation of the physical mechanism of induced seismicity with and without pore pressure perturbation (Tang et al., 2018; Zhou et al., 2019), respectively. To verify the two physical mechanisms, geomechanical modeling must realistically account for the coupling of flow and poromechanical responses. This motivates us to develop a fully-coupled model based on linear poroelasticity, whose governing equations are elaborated in SM-S5.

A finite element model based on COMSOL Multiphysics (version 5.3a) was used to simulate the deformation and flow. The 2D mesh of triangular elements was highly refined for the reservoir layer, faults, injection sources, and intersecting points to resolve large stress and pressure gradients (Fig. S9). Because our focus is on the perturbation of stresses and flow associated with gas injection and extraction, it is reasonable to prescribe no-flow and stress-free conditions on the lateral and lower boundaries at large distances from the repository (Fig. 5). We also prescribed the surface to be stress-free water table. The repository boundaries were set as aforementioned.

## 5. Model calibration and simulation

From a hydrological perspective our geomechanical model is made up of two domains that can be idealized as hydraulically isolated from one another. The upper domain consists of the two upper aquifers underlain by the Upper Layer 3 and caprock with permeabilities two to six orders of magnitude lower (Table 1), which hydraulically shield it from the lower domain. Because the reservoir layer in the lower domain is sandwiched between the basal layers and caprock with permeabilities at least two to four orders of magnitude lower, it has little hydraulic connection with the upper aquifers.

The hydrogeologic framework has significant influence on the development of deformation and stress. In this section, we first considered the surface deformation associated with two scenarios: withdrawal of groundwater from the surface aquifer, and cyclic gas injection-extraction of the HUGS. The two analyses allow us to use vertical and horizontal components of GPS displacements to constrain the permeability of the upper aquifers and the reservoir hydraulic properties, respectively. We then in a further analysis used the geomechanical model so calibrated to simulate the deformation and stress perturbation resulting from the HUGS activities.

### 5.1. Constraining the permeability of upper aquifers

At a distance of ~2 km from the HUGS center is a water well (H5) penetrating 100 m depth (Fig. S1b), whose level has been monitored since 2014. The GPS station (HP12) is located at 83 m from it. Primarily for irrigation, the well each year undergoes a cyclic change in level, dropping to a minimum during the summer when withdrawal of water is at a maximum. The well level and uplift data were analyzed by Qiao et al. (2018), who concluded that the cyclic changes of well level and vertical uplift were positively correlated, with a time lag remained about the same from year to year. During summer after the well level had dropped to a minimum, the vertical subsidence would continue to increase and not attain its annual maximum until ~20 days later. Because of the variability of the hydrologic cycle and irrigation need, amplitudes of the well level change and uplift would fluctuate with years. Here we focused on the period from 15 November 2015 to 24 March 2017, during which the most pronounced changes were observed: a significant uplift of >3 cm developed in response to well level change of ~20 m (Fig. 6a).

We used our geomechanical model to simulate the uplift that would result from the observed well level change with the assumption that both flow and deformation in the relatively thin unsaturated zone near the surface can be approximated as those in a saturated state (SM-S6). Through increasing the permeability of aquifers from 10<sup>-15</sup> to 10<sup>-13</sup> m<sup>2</sup>, the RMS misfits between the predicted and observed vertical displacements range from 0.89 to 0.37 cm (Fig. 6b). To avoid over- or under-fitting, the RMS fitting residual should be close to the average observation error of 0.5 cm. Accordingly, our geomechanical modeling together with the GPS and well data constrained the permeability of the two aquifers to be two alternative optimal values of 1.3 and 7.5 × 10<sup>-14</sup> m<sup>2</sup>, which are consistent with the permeability ranges of the formation rocks (Table S2) (Freeze and Cherry, 1979).

Our simulated results agree qualitatively with what are expected of transient flow in well hydraulics (Freeze and Cherry, 1979). From dimensional analysis the hydraulic-head drawdown near the well should scale directly with the pumping rate and inversely with the transmissivity (directly proportional to permeability). This therefore implies that the drawdown would be less for an aquifer with larger permeabilities under the same pumping rate. In other words, to achieve a drawdown in a more permeable aquifer, the pumping rate needs to be higher, which would induce

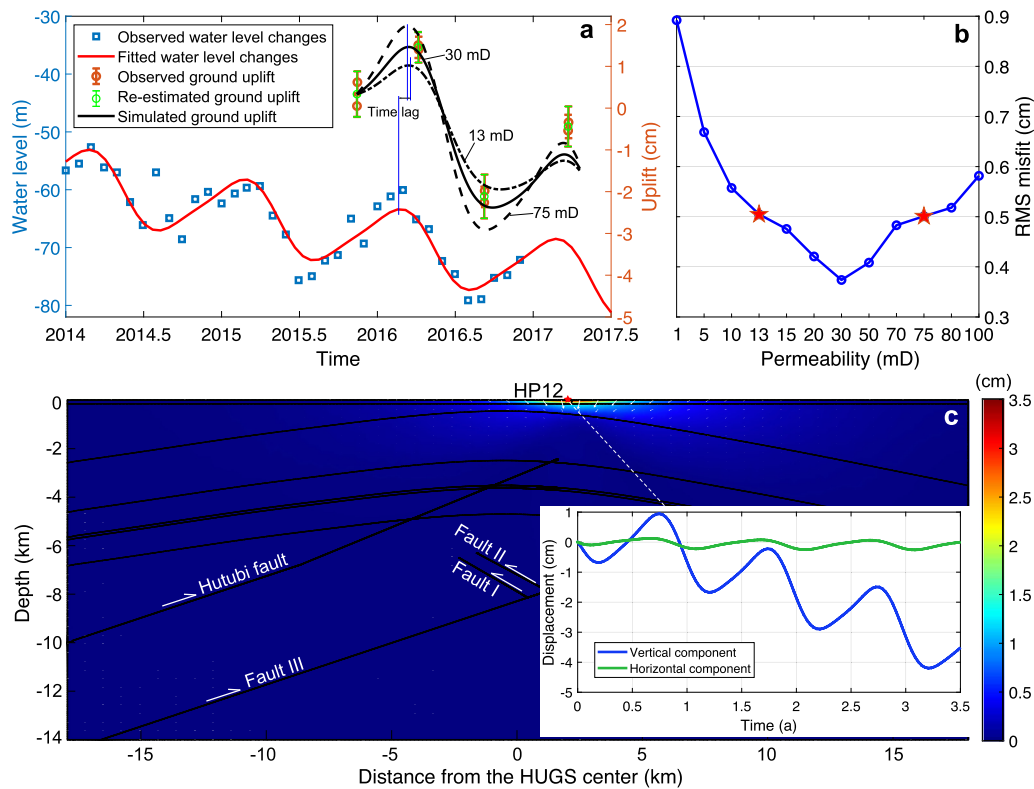


**Fig. 6.** Surface displacements due to groundwater withdrawal in Upper Aquifers 1-2 with different permeabilities. (a) Groundwater level changes of well H5 and ground vertical displacements at station HP12. Vertical blue lines mark the time lag among peak well level and maximum surface uplifts. The re-estimated ground uplifts are based on the fluctuation ranges of the vertical displacements of each observation. (b) Varying RMS misfits to the vertical displacements with different permeabilities. Red stars denote the two permeabilities of  $1.3$  and  $7.5 \times 10^{-14} \text{ m}^2$  with RMS misfits close to the observation error. (c) Cumulative displacements after groundwater pumping of 3.5 years using the fitted water level changes (red curve in panel a) under the preferred permeability of  $7.5 \times 10^{-14} \text{ m}^2$ . The inset shows the horizontal and vertical displacements at station HP12.

larger loss of pore fluid and more pronounced compaction (and volumetric strain). In an aquifer or hydrocarbon reservoir with a very large lateral extent, it is generally observed that compaction from fluid withdrawal is dominated by the vertical strain, with minimal lateral strains (Geertsma, 1973; Segall et al., 1994; Walsh, 2002), as shown in Figs. 6c and S10 (with multiple pumping wells). Accordingly, one expects the vertical strain and displacements to correlate with the drawdown, with a magnitude increasing with permeability (Fig. 6a).

Because the transient flow in response to pumping is a diffusion phenomenon, the temporal change of pore pressure and deformation typically lags behind the pumping history, with a characteristic time  $\tau$  that scales with the square of the characteristic distance ( $\ell^2$ ) divided by the hydraulic diffusivity  $\kappa = k/(\eta S_e)$  (also directly proportional to permeability).  $\eta$  and  $S_e$  are the fluid viscosity and the constrained specific storage, respectively. It then follows that if the distance (between the well and GPS station) is fixed, then the characteristic time lag is expected to scale inversely with permeability, as shown in our simulations (Fig. 6a).

## 5.2. Constraining the reservoir porosity and permeability

The next scenario to consider is the cyclic gas injection-extraction of the HUGS. Wellhead pressure and horizontal ground extension were analyzed together with geomechanical modeling to constrain the porosity and permeability of the reservoir layer. As for the earlier scenario most of the hydromechanical parameters were fixed as specified in Table 1 with setting an optimal permeability of  $7.5 \times 10^{-14} \text{ m}^2$  for the two aquifers. Actually, the aquifers are hydraulically isolated from the reservoir layer, their permeabilities have little impact on the simulation of cyclic gas

injection-extraction. However, for the reservoir layer, we considered large ranges of porosity (from 3% to 30%) and permeability (from  $10^{-17} \text{ m}^2$  to  $10^{-12} \text{ m}^2$ ) from well logging data and rock physics experiments.

We developed a grid-search method to pinpoint optimum values of porosity and permeability for the reservoir layer jointly using the pressure and GPS data (SM-S7). After simulating cyclic gas injection-extraction from 9 June 2013 to 30 April 2017, we compared the model predictions with the observed bottom-hole pressure changes and four displacement profiles. Also based on the same fitting criteria as described in Section 5.1, the RMS residuals should be comparable to the observation errors (0.41 cm for ground extension and 1.87 MPa for pressure changes). The residual of pressure changes exhibits a closed contour with the RMS misfit equal to the observation error (Fig. 7a). By comparison, ground extension is more sensitive to the porosity than the permeability (Fig. 7b). Around the 1.87-MPa contour, all the RMS misfits of displacements range from 0.37 to 0.38 cm, slightly less than the average error of the four extension profiles. Consequently, together with our modeling, the observed pressure changes and ground extension constrained the reservoir porosity and permeability to fall on very narrow ranges of 20-30% and  $1.25\text{-}3.25 \times 10^{-13} \text{ m}^2$ , respectively, which are in accord with the previous results from analyses of the reservoir characteristics and properties (Song and Hu, 2001; Li et al., 2014) and supported by sensitivity analysis (SM-8).

Again our simulated results on how porosity and permeability can influence the downhole pressure and ground displacement agree with what one would expect of transient flow and poroelasticity (Freeze and Cherry, 1979; Segall, 2000). The injection of a volume of gas into the HUGS instantaneously increases the downhole pressure in the well, and how this localized per-

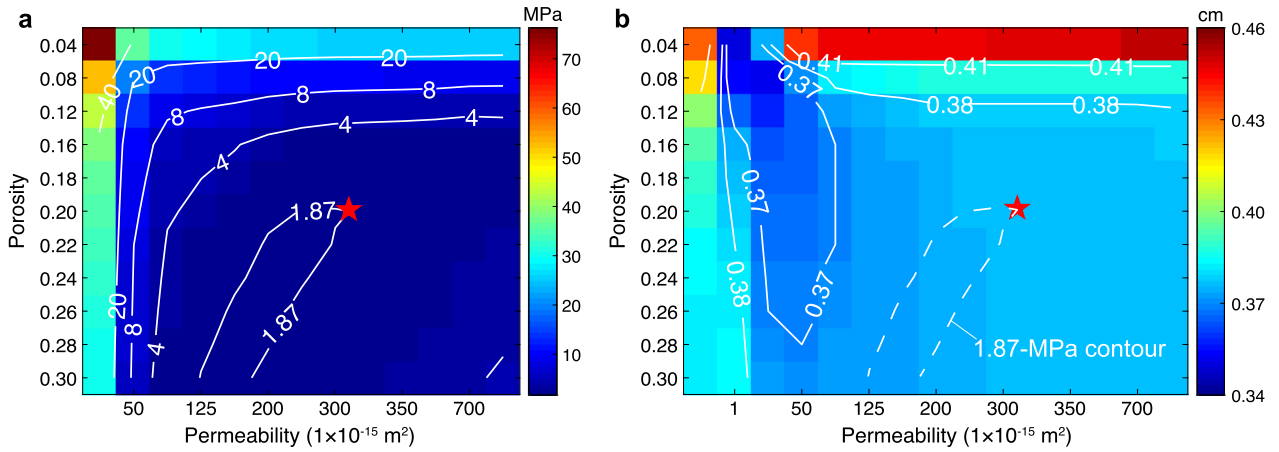


**Fig. 7. Grid searching results of the reservoir porosity and permeability under constraints from the bottom-hole pressure changes and four horizontal ground extension profiles.** (a) RMS misfits to the pressure changes with contours. The RMS misfits at the permeabilities of 0.1 and  $1 \times 10^{-15} \text{ m}^2$  are not shown due to extremely large values of 170 to 1800 MPa. (b) RMS misfits to the extension profiles with contours. Red stars denote the parameters adopted in Sections 5.3 and 5.4.

turbation would dissipate is controlled by the hydraulic diffusivity. This implies that for a given injection/extraction history, the corresponding change in downhole pressure would decrease with permeability. Porosity may also have a minor influence through its connection with the specific storage  $S_e$ . Given that the surface formations are hydraulically isolated from the reservoir layer, appreciable ground displacement related to gas injection could be only developed by poroelastic deformation due to the enhancement of pore pressure. For a given injection volume, the pressure enhancement would likely decrease with porosity (Segall, 2000). This implies that magnitude of the ground displacements would also decrease with porosity.

### 5.3. Simulation results of ground displacements and pressure changes

Based on the results from Sections 5.1 and 5.2, we conducted forward modeling of the downhole pressure and displacement field using optimum values for aquifer permeability ( $7.5 \times 10^{-14} \text{ m}^2$ ) as well as reservoir porosity (20%) and permeability ( $3.25 \times 10^{-13} \text{ m}^2$ ). The injection-extraction history up to 30 April 2017 was simulated using the mean production data described in Section 2.2. Spatiotemporal development of the displacements is presented in the supplementary Video S1, and the cumulative displacements at the end of the fourth injection phase are presented in Fig. 8a. In response to the pressure increase within the HUGS, the surrounding rock expands and results in extensional displacements on the order of 1 cm that radiate from the repository. The magnitude decreases with radial distance. Symmetry constrains the displacements at locations vertically above the repository center to align in a vertical direction, with negligible horizontal component. At the surface the horizontal displacement vanishes at the central location and increases with distance away from the center, reaching a maximum at  $\sim 3 \text{ km}$  before decaying gradually to vanish at large distances.

Temporal development of the horizontal and vertical components of the ground displacements at three lateral distances are presented in Fig. 8b. The maximum horizontal extension is predicted to be  $\sim 0.27 \text{ cm}$  at 3 km, which would decrease to  $\sim 0.17 \text{ cm}$  at 6 km. In contrast, the uplift has a maximum at the center, with a magnitude of  $\sim 0.22 \text{ cm}$  that would decrease laterally down to  $\sim 0.10 \text{ mm}$  at 6 km. Because such vertical displacements induced by gas injection are much smaller than that due to groundwater withdrawal by orders of magnitude, our GPS data for uplift were probably dominated by the latter (Qiao et al., 2018). On the other hand, as explained above in Section 5.1, the horizontal strains associated with such hydrological processes are expected to be negligible in an aquifer that extends laterally over long distances, which

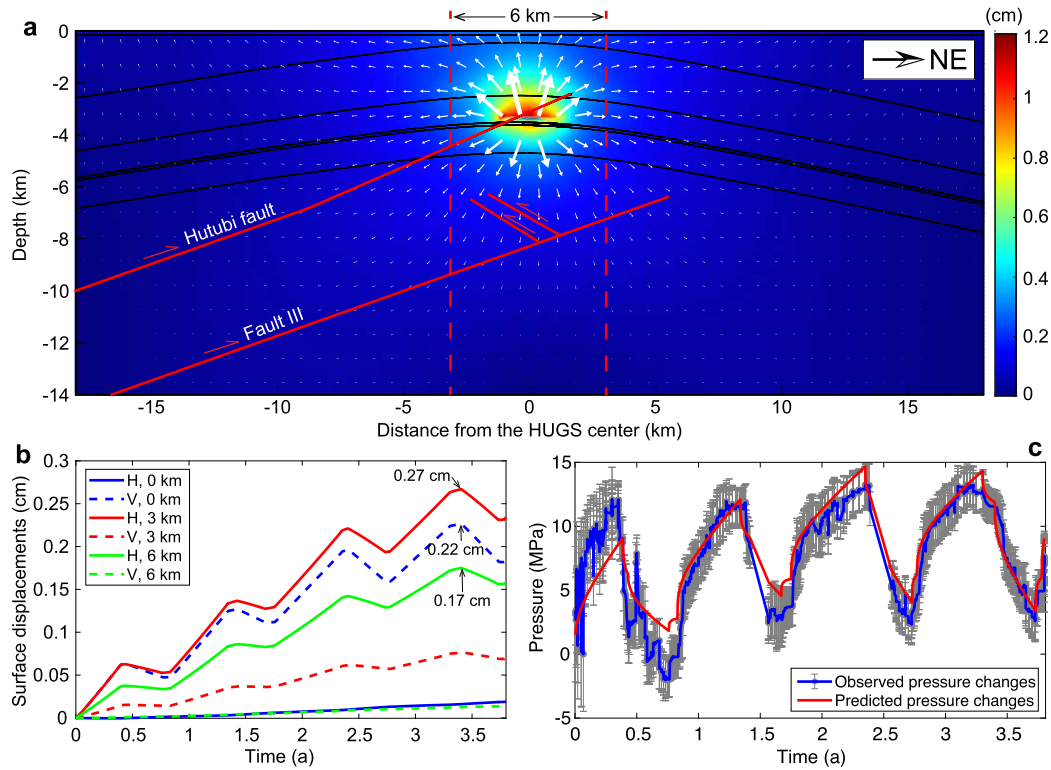
implies that we can readily rule out the withdrawal of groundwater as causally related to the extensile strains that were appreciable in the GPS data. Our geomechanical modeling corroborates quantitatively that poroelastic deformation associated with cyclic injection-extraction of the HUGS can explain both the magnitude and spatiotemporal evolution of the horizontal displacement field.

Fig. 8c presents simulated bottom-hole pressure changes, which are in good agreement with the well data derived from the mean pressure changes in Fig. 2e by subtracting the initial pressure on 9 June 2013. Due to the absence of gas production data of the first gas injection-extraction cycle, the pressure fit is not as good as the other three cycles. The bottom-hole pressure increased during the first three injection phases and peaked at  $\sim 28 \text{ MPa}$  at the ends of the third and fourth injection phases, with a gap of  $\sim 6 \text{ MPa}$  to reach the maximum working pressure. Video S2 shows spatiotemporal diffusion of pore pressure, whose change was confined within the gas reservoir. During short extraction phases, the pressure drop was abrupt and localized near the wells, without sufficient time to diffuse to the far ends of the repository. In contrast, the injection phase extended over a sufficiently long time for the pressure enhancement to spread throughout the repository.

### 5.4. Simulation results of Coulomb stress perturbation

As introduced earlier in Section 1, due to the absence of detailed hydrogeological and geomechanical modeling, the two distinct physical mechanisms of induced seismicity proposed by Tang et al. (2018) and Zhou et al. (2019) are qualitative conclusions. Benefiting from more seismological data, Zhou et al. (2019) were able to better resolve the location and spatial clustering of the events associated with the first and second injection phases in the study area, and most importantly, to derive the focal mechanism solutions of the two largest events. These new solutions provided us with the critical links for simulating Coulomb stress perturbation and potential for seismic hazards in the HUGS seismogenic system.

The focal mechanisms indicate that the two largest earthquakes are characterized by thrust-slip on faults dipping to southwest at angles of  $17^\circ$  and  $25^\circ$ , respectively, which are comparable to the Hutubi fault and Fault III shown in the seismic profiles (Fig. 4). The inferred style of faulting is also compatible with the regional tectonic setting characterized by overall northeast-southwest compression (Lu et al., 2018). Based on these results, we simulated the Coulomb stress perturbation with the same hydromechanical parameters adopted in Section 5.3. The equation of Coulomb stress is provided in SM-S9. We assumed the putative receiver faults to



**Fig. 8.** Simulation results of displacements and bottom-hole pressure changes induced by cyclic gas injection-extraction of the HUGS. (a) Predicted displacements at the end of the fourth injection phase colored by magnitude. White arrows represent the displacement vector. Two red dashed lines mark the positions with the maximum ground extension. (b) Time-dependent ground displacements at 0, 3, and 6 km from the center of the HUGS. H: horizontal displacements; V: vertical displacements. (c) Bottom-hole pressure changes since 9 June 2013 with the predicted results.

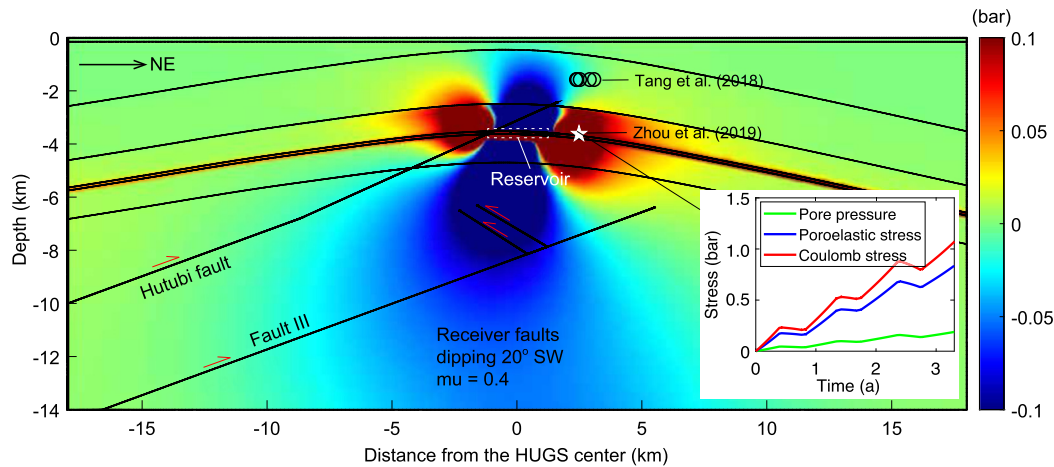


**Fig. 9.** Coulomb stress perturbation at the end of the fourth injection phase induced by cyclic gas injection-extraction of the HUGS. Black circles show the five  $M_L \geq 3.0$  earthquakes in Fig. 1c relocated by Tang et al. (2018). The white star marks the location of the seismic cluster in August 2013 from Zhou et al. (2019). Inset figure plots the temporal changes of pore pressure, poroelastic and Coulomb stresses at the location of the seismic cluster.

be southwest-dipping with an angle of 20°, and the friction coefficient was fixed at 0.4.

Fig. 9 shows the spatial distribution of Coulomb stress perturbation (termed as  $\Delta CFS$ ) at the end of the fourth injection phase. The magnitude is on the order of 0.1 bar, considered to be sufficiently large to induce earthquakes if the tectonic stress field is closed to failure. There are two lobes with elevated  $\Delta CFS$  located on either side of the HUGS. The seismic cluster in August 2013 with the two largest earthquakes determined by Zhou et al. (2019) fall on the northeast lobe. In contrast, the relatively shallow hypocenter locations of Tang et al. (2018) fall in a region of negative  $\Delta CFS$ . Therefore, our modeling here is in better agreement with the seis-

micity distribution relocated by Zhou et al. (2019) with more local stations. Besides, stress variation at the location of the earthquake cluster (white star in Fig. 9) reveals that pore pressure increased very little and that the enhancement of Coulomb stress was mainly due to poroelastic effect.

## 6. Discussion and conclusions

### 6.1. Merits and demerits

Although hundreds of underground repositories for natural gas have been established worldwide, limited observation and systematic analysis on seismicity possibly induced by the cyclic injection

and extraction of gas that typically occurs on an annual basis in such facilities. The Hutubi repository is unique, as relatively comprehensive data from seismological and geodetic networks have been acquired over multiple cycles of injection and extraction. The seismological (Tang et al., 2018; Zhou et al., 2019) and geodetic (Qiao et al., 2018) data have helped establish a causal relationship between the injection/extraction activity and occurrence of earthquakes, and these recent analyses also suggested possible mechanisms for induced seismicity in the study area. However, they also underscored that, if one strives to arrive at a deeper quantitative understanding, it is necessary to develop a physically based geomechanical model that is guided and constrained by the hydrogeologic and geophysical data.

To set up the hydrogeologic framework and specify hydromechanical parameters of our geomechanical model, we synthesized a variety of data, including seismic reflection profiles, local velocity model, rock physics measurements, well drilling and logging data. From a hydrological perspective, our geomechanical model is made up of two domains that can be considered as hydraulically shielded from each other. In particular, the repository has limited hydraulic connection with either the surface or inferred locations of the induced earthquakes. Therefore, the interactions among the domains and their constituent layers can only be realistically captured with a geomechanical model based on fully-coupled poroelasticity. Predictions of our model agree well with the observed ground extension and well pressure data, which were used to refine the reservoir hydraulic properties. Our study here shows that these fields are sensitive to the pumping rates and time scales of injection and extraction, which need to be analyzed systematically for safe design of the repository. It should be noted that our model still has several limitations as it is a 2D formulation with constant fluid viscosity and bulk modulus (see more discussion in SM-S10).

### 6.2. Implications for geodetic measuring and modeling

There have been a few studies incorporating geodetic observations into the seismological and geomechanical analyses of induced seismicity (Vasco et al., 2010, 2013; Shirzaei et al., 2016 and 2019), and they all focused on the vertical ground displacements. Because the vertical deformation in the study area was predominately due to hydrological processes (Qiao et al., 2018), here we instead paid attention to the horizontal ground displacements. Our analysis shows that both magnitudes of the horizontal displacements and strain as well as their spatial localization reasonably agree with what would be expected at locations immediately above the repository. Our GPS observations were able to resolve ground extension and shortening on the order of cm in response to injection and extraction of gas from the repository at depth. Especially, our simulation results reveal that the horizontal ground extension is larger than uplift. The significant implication is that ground displacements induced by fluid injection into deep reservoirs can be observed in a region even suffering from groundwater withdrawal simultaneously, considering high precision of GPS horizontal observations and negligible horizontal deformation associated with shallow hydrological processes.

Although ground displacements have often been used to analyze deformation related to natural earthquakes and volcanic activities (Segall, 2000), our study represents one of the first attempts to successfully connect horizontal geodetic data with gas injection and induced seismicity. Particularly, we also developed a grid-search technique to derive optimal estimates of permeability and porosity of the reservoir, constrained by the ground extension and well pressure data. Our study would suggest the potential of adopting a similar approach utilizing horizontal displacement data to other gas injection sites. However, it should also be noted that

having data for multiple cycles in this instance has allowed us to perform a relatively robust analysis at the HUGS.

### 6.3. Physical mechanism of induced seismicity

Guided by our seismic profiles and the new findings of Zhou et al. (2019), we simulated the Coulomb stress perturbation, and our analysis has provided useful insights into the connection with the HUGS activities and potentially induced earthquakes. As the HUGS reservoir was dilating during cyclic gas injection-extraction (Video S1) and the increase of pore pressure in the two stressing lobes is little (Fig. 9 and Video S2), the positive  $\Delta CFS$  is attributed to the reservoir dilation that extrudes the surrounding region. Based on above quantitative analysis, the observed seismicity was probably induced by the poroelastic effect (resulting from the reservoir dilation) exerting on neighboring faults without hydraulic connection to the repository, which supports the physical mechanism proposed by Zhou et al. (2019).

The geomechanical model has been used to simulate development of the displacement field and downhole pressure associated with four cycles of injection and extraction. Having calibrated our model, the next step is to analyze in more details the cyclic spatiotemporal evolution of  $\Delta CFS$ , as well as its sensitivity to parameters including fault angles, friction and Biot coefficients. The rate of stress perturbation and its potential connection with induced seismicity should also be considered. A comprehensive investigation of these important issues is beyond the scope of the present study, but it is our intention to tackle them in the future.

### Declaration of competing interest

The authors are not aware of any competing interests.

### Acknowledgements

We greatly appreciate PetroChina for providing seismic profiles and drilling data, and PetroChina Xinjiang Oilfield Branch for gas production and wellhead pressure data. The well logging data are provided by the Xinjiang Branch of PetroChina Logging Company. We thank Zhanbo Ji and Pengcheng Zhou for providing the local velocity model and the relocated earthquake data, respectively. We also would like to thank Manoochehr Shirzaei and another anonymous reviewer for constructive comments. This study was supported by the NSFC/RGC Joint Research Scheme (N\_CUHK418/15, N\_CUHK430/16, and 41561164018), the Hong Kong Scholars Program and CUHK Research Fellowship Scheme (4200555). X.Q. and X.W. were funded by NSFC General Programs (Nos. 41474097 and 41474016). **Data and materials availability:** All data needed to evaluate the conclusions in the paper are present in the paper and/or the Supplementary Material.

### Appendix A. Supplementary material

Supplementary material related to this article can be found online at <https://doi.org/10.1016/j.epsl.2019.115943>.

### References

- Bao, X., Eaton, D.W., 2016. Fault activation by hydraulic fracturing in western Canada. *Science* 354 (6318), 1406–1409.
- Barbour, A.J., Evans, E.L., Hickman, S.H., Eneva, M., 2016. Subsidence rates at the southern Salton Sea consistent with reservoir depletion. *J. Geophys. Res.* 121, 5308–5327. <https://doi.org/10.1002/2016JB012903>.
- Bjørnarå, T.I., Nordbotten, J.M., Park, J., 2016. Vertically integrated models for coupled two-phase flow and geomechanics in porous media. *Water Resour. Res.* 52, 1398–1417. <https://doi.org/10.1002/2015WR017290>.
- Brocher, T.M., 2005. Empirical relations between elastic wave speeds and density in the Earth's crust. *Bull. Seismol. Soc. Am.* 95, 2081–2092.

- Cao, X., 2013. A Research on Reservoir Geomechanics Features of a Gas Storage in Xinjiang After Natural Depletion. Ph.D. thesis. China University of Geoscience, Beijing.
- Deng, Q.D., Feng, X.Y., Yang, X.P., 1994. Study on Holocene paleoearthquake by large trench in the Manas-Tugulu reverse fault- and-fold zone along Northern margin of the Tianshan mountain in Xinjiang. In: Institute of Geology, SSB (Eds.), Research on Active Faults, vol. 3. Seismological Press, Beijing, China (in Chinese).
- Deng, Q.D., Feng, X.Y., Zhang, P.Z., Xu, X.W., Yang, X.P., Peng, S.Z., 1996. Paleoseismology in the northern piedmont of Tianshan Mountains, Northwestern China. *J. Geophys. Res.* 101, 5895–5920.
- Deng, Q., Ran, Y., Yang, X., Min, W., Chu, Q., 2007. Map of Active Tectonics in China. Seismological Press, Beijing.
- Fialko, Y., Simons, M., 2000. Deformation and seismicity in the Coso geothermal area, Inyo County, California: observations and modeling using satellite radar interferometry. *J. Geophys. Res.* 105, 21,781–21,793.
- Foulger, G.R., Wilson, M.P., Gluyas, J.G., Julian, B.R., Davies, R.J., 2018. Global review of human-induced earthquakes. *Earth-Sci. Rev.* 178, 438–514.
- Freeze, R.A., Cherry, J.A., 1979. Groundwater. Prentice-Hall Inc., Englewood Cliffs.
- Gaite, B., Ugalde, A., Villaseñor, A., Blanch, E., 2016. Improving the location of induced earthquakes associated with an underground gas storage in the Gulf of Valencia (Spain). *Phys. Earth Planet. Inter.* 254, 46–59.
- Gan, W., Frohlich, C., 2013. Gas injection may have triggered earthquakes in the Cogdell oil field, Texas. *Proc. Natl. Acad. Sci.* 110 (47), 18786–18791.
- Geertsma, J., 1973. A basic theory of subsidence due to reservoir compaction: the homogeneous case. *Verh. K. Ned. Geol. Mijnbouwkd* 28, 43–62.
- Herrmann, R.B., 2013. Computer programs in seismology: an evolving tool for instruction and research. *Seismol. Res. Lett.* 84, 1081–1088. <https://doi.org/10.1785/0220110096>.
- Hu, G., Zhang, S., Li, J., Li, J., Han, Z., 2010. The origin of natural gas in the Hutubi gas field, Southern Junggar Foreland Sub-basin, NW China. *Int. J. Coal Geol.* 84, 301–310.
- Ji, Z., Wang, B., Wang, H., Wang, Q., Su, J., 2017. Seismic velocity and its temporal variations of Hutubi Basin revealed by near surface trapped waves. In: AGU Fall Meeting Abstracts. 2017.
- Juanes, R., Castineira, D., Fehler, M.C., Hager, B.H., Jha, B., Shaw, J.H., Plesh, A., 2017. Coupled flow and geomechanical modeling, and assessment of induced seismicity, at the Castor underground gas storage project. Final report. [http://mesadelaria.es/documentos/20170424\\_Castor\\_final\\_report\\_final\\_signed.pdf](http://mesadelaria.es/documentos/20170424_Castor_final_report_final_signed.pdf).
- Keranen, K.M., Weingarten, M., Abers, G.A., Bekins, B.A., Ge, S., 2014. Sharp increase in central Oklahoma seismicity since 2008 induced by massive wastewater injection. *Science* 359, 448–451.
- Keranen, K.M., Weingarten, M., 2018. Induced seismicity. *Annu. Rev. Earth Planet. Sci.* 2018 (46), 149–174.
- Laske, G., Masters, G., Ma, Z., Pasyanos, M., 2013. Update on CRUST1.0—a 1-degree global model of Earth's crust. *Geophys. Res. Abstr.* 15, Abstract EGU2013-2658.
- Li, Y., Li, Y., Gao, Q., Wang, B., Li, D., Pang, J., Li, W., 2014. New understanding of reservoir of Z2 sand layer of Ziniquanzi formation in Hutubi gas storage. *Xinjiang Petroleum Geol.* 35 (2), 182–186.
- Lu, R., He, D., Xu, X., Wang, X., Tan, X., Wu, Xi., 2018. Seismotectonics of the 2016 M 6.2 Hutubi earthquake: implications for the 1906 M 7.7 Manas earthquake in the northern Tianshan belt, China. *Seismol. Res. Lett.* 89 (1), 13–21.
- Ludwig, W.J., Nafe, J.E., Drake, C.L., 1970. Seismic refraction. In: Maxwell, A.E. (Ed.), *The Sea*, vol. 4. Wiley-Interscience, New York, pp. 53–84.
- Majer, E.L., et al., 2007. Induced seismicity associated with enhanced geothermal systems. *Geothermics* 36, 185–222.
- Mogi, K., 1958. Relations between the eruptions of various volcanoes and the deformations of the ground surfaces around them. *Bull. Tokyo Earthq. Res. Inst.* 36 (2), 99–134.
- Mossop, A., Segall, P., 1997. Subsidence at the Geysers geothermal field, N. California from a comparison of GPS and leveling surveys. *Geophys. Res. Lett.* 24 (14), 1839–1842.
- Pang, J., Qian, G., Wang, B., Yang, Z., Wei, Y., Li, Y., 2012. Evaluation of sealing ability of underground gas storage converted from the Xinjiang H gas field. *Nat. Gas Ind.* 32 (2), 1–3.
- Qiao, X., Chen, W., Wang, D., Nie, Z., Chen, Z., Li, J., Wang, X., Li, Y., Wang, T., Feng, G., 2018. Crustal deformation in the Hutubi underground gas storage site in China observed by GPS and InSAR measurements. *Seismol. Res. Lett.* 89 (4), 1467–1477.
- Schultz, R., Atkinson, G., Eaton, D.W., Gu, Y.J., Kao, H., 2018. Hydraulic fracturing volume is associated with induced earthquake productivity in the Duvernay play. *Science* 359, 304–308.
- Segall, P., Grasso, J.-R., Mossop, A., 1994. Poroelastic stressing and induced seismicity near the Lacq gas field, southwestern France. *J. Geophys. Res.* 99, 15,423–15,438.
- Segall, P., 1989. Earthquakes triggered by fluid extraction. *Geology* 17, 942–946.
- Segall, P., 2000. Earthquake and Volcano Deformation. Princeton Univ. Press, Princeton, N. J.
- Shaw, J.H., Connors, C., Suppe, J., 2005. Seismic Interpretation of Contractual Fault-Related Folds: An AAPG Seismic Atlas. American Association of Petroleum Geologists, Tulsa, pp. 1–156.
- Shirzaei, M., Ellsworth, W.L., Tiampo, K.F., González, P.J., Manga, M., 2016. Surface uplift and time-dependent seismic hazard due to fluid injection in eastern Texas. *Science* 353 (6306), 1416–1419.
- Shirzaei, M., Manga, M., Zhai, G., 2019. Hydraulic properties of injection formations constrained by surface deformation. *Earth Planet. Sci. Lett.* 515, 125–134.
- Skoumal, R.J., Brudzinski, M.R., Currie, B.S., Levy, J., 2014. Optimizing multi-station earthquake template matching through re-examination of the Youngstown, Ohio sequence. *Earth Planet. Sci. Lett.* 405, 274–280.
- Song, Y., Hu, X., 2001. Characteristics and comprehensive evaluation of Ziniquanzi reservoir. *J. Xi'an Pet. Inst. (Nat. Sci. Edn.)* 16 (4), 15–19.
- Tang, L., Lu, Z., Zhang, M., Sun, L., Wen, L., 2018. Seismicity induced by simultaneous abrupt changes of injection rate and well pressure in Hutubi gas field. *J. Geophys. Res., Solid Earth* 123 (7), 5929–5944. <https://doi.org/10.1029/2018JB015863>.
- Thienen-Visser, K., Breunese, J.N., 2015. Induced seismicity of the Groningen gas field: history and recent developments. *Leading Edge*, 664–671.
- Vasco, D.W., Rucci, A., Ferretti, A., Novali, F., Bissell, R.C., Ringrose, P.S., Mathieson, A.S., Wright, I.W., 2010. Satellite-based measurements of surface deformation reveal fluid flow associated with the geological storage of carbon dioxide. *Geophys. Res. Lett.* 37, L03303. <https://doi.org/10.1029/2009GL041544>.
- Vasco, D.W., Rutqvist, J., Ferretti, A., Rucci, A., Bellotti, F., Dobson, P., Oldenburg, C., Garcia, J., Walters, M., Hartline, C., 2013. Monitoring deformation at The Geysers Geothermal Field, California using C-band and X-band interferometric synthetic aperture radar. *Geophys. Res. Lett.* 40, 2567–2572. <https://doi.org/10.1002/grl.50314>.
- Verdon, J.P., Kendall, J.-M., Stork, A.L., Chadwick, R.A., White, D.J., Bissell, R.C., 2013. Comparison of geomechanical deformation induced by megaton-scale CO<sub>2</sub> storage at Sleipner, Weyburn, and In Salah. *Proc. Natl. Acad. Sci.* 110, E2762–E2771.
- Verdon, J.P., Kendall, J.-M., White, D.J., Angus, D.A., 2011. Linking microseismic event observations with geomechanical models to minimise the risks of storing CO<sub>2</sub> in geological formations. *Earth Planet. Sci. Lett.* 305, 143–152.
- Verdon, J.P., Stork, A.L., Bissell, R.C., Bond, C.E., Werner, M.J., 2015. Simulation of seismic events induced by CO<sub>2</sub> injection at In Salah, Algeria. *Earth Planet. Sci. Lett.* 426, 118–129.
- Wang, C.Y., Yang, Z.E., Luo, H., Mooney, W.D., 2004. Crustal structure of the northern margin of the eastern Tien Shan, China, and its tectonic implications for the M ~7.7 Manas earthquake. *Earth Planet. Sci. Lett.* 223, 187–202.
- Wang, H., 2000. Theory of Linear Poroelasticity with Applications to Geomechanics and Hydrogeology. Princeton Univ. Press, Princeton, N. J.
- Walsh, J.B., 2002. Subsidence above a planar reservoir. *J. Geophys. Res.* 107 (B9), 2202. <https://doi.org/10.1029/2001JB000606>.
- Yang, H., Liu, Y., Wei, M., Zhuang, J., Zhou, S., 2017. Induced earthquakes in the development of unconventional energy resources. *Sci. China Earth Sci.* 60 (9), 1632–1644. <https://doi.org/10.1007/s11430-017-9063-0>.
- Zhou, P., Yang, H., Wang, B., Zhuang, J., 2019. Seismological investigations of induced earthquakes near the Hutubi underground gas storage. *J. Geophys. Res., Solid Earth.* <https://doi.org/10.1029/2019JB017360>.